Chemical Science

ROYAL SOCIETY OF CHEMISTRY

EDGE ARTICLE

View Article Online
View Journal | View Issue

Cite this: *Chem. Sci.*, 2024, **15**, 16156

All publication charges for this article have been paid for by the Royal Society of Chemistry

A nanocarbon-enabled hybridization strategy to construct pharmacologically cooperative therapeutics for augmented anticancer efficacy†

Huan Wang,[a] Xinchen Liu,[b] Xiangyu Yan,[c] Yong Du,[c] Fang Pu,[a] Jinsong Ren *[a] and Xiaogang Qu *[a]

The drug design principles are of great value in developing nanomedicines with favorable functionalities. Herein we propose a nanocarbon-enabled hybridization strategy to construct a pharmacologically cooperative nanodrug for improved cancer therapy in the light of pharmacophore hybridization in medicinal chemistry and the synthetic principles of nanocarbons. An antioxidant defense pharmacological inhibitor and a co-nucleation precursor are structurally hybridized into nanodrugs (SCACDs) *via* forming carbon quantum dots. These SCACDs elicit dual enhanced bioactivities, including superior sonocatalytic activity that arose from the appropriate band structure of the pharmacophoric carbon cores, and more than an order of magnitude higher antioxidant defense inhibitory activity than the pharmacological inhibitor *via* conveying the bioactive pharmacophores from the molecular level to nanoscale. *In vivo*, SCACDs possess a long body retention and desirable biodistribution to eliminate melanoma cells at a very low injection dose. The present study provides a viable yet effective strategy for the development of pharmacologically cooperative nanodrugs to achieve remarkably improved therapeutic efficacy.

Received 7th August 2024
Accepted 2nd September 2024

DOI: 10.1039/d4sc05280c

rsc.li/chemical-science

Introduction

Pharmacophore hybridization has been regarded as an effective approach in medicinal chemistry to realize improved therapeutic outcomes *via* the combination of two distinct pharmacophoric moieties that have different but cooperative bioactivities into a new hybrid scaffold.[1–3] Through the fusion of pharmacologically active domains of the known drugs, such a powerful approach has shown great promise for treating various diseases such as bacterial infections, viral infections, and malaria, as well as cancer to overcome drug resistance or increase the pharmacological efficacy of parent drugs.[4–10] Importantly, a single hybrid medication with a dual mode of action shows pharmacokinetic advantages over the co-administration of two distinct parent drugs by possessing a simpler pharmacokinetic profile, avoiding the differences in pharmacokinetics of parent drugs, drug–drug interactions, and adverse reactions. However, roadblocks regarding poor water solubility, short body retention, and low specificity of small molecule hybrid medicines lead to diminished therapeutic efficacy. Such dilemmas in drug development can be overcome by referring to the principles of nanomedicine that focus on drug delivery.[11–14] Yet, nanocarriers used for drug delivery usually raise safety concerns caused by the increased dosing requirements due to the limited cargo loading capacity and complex drug–carrier interactions.[15–17] Recently, drug self-delivery systems manufactured *via* molecular self-assembly strategies can realize the delivery of drug combinations without the aid of additional nanocarriers.[18–25] Nonetheless, shortcomings including the insufficient bio-stability and lack of self-assembly potential of required pharmaceutical ingredients still remain and hinder further translation.[26,27] Thus, alternative but effective strategies are urgently needed for the construction of nanodrugs with cooperative bioactivities for advanced efficacy.

Zero-dimensional carbon quantum dots (CQDs) have attracted great attention in nanomedicine due to their widespread sources, high bio-stability, nontoxicity, and long body retention.[28–32] In particular, the precursor-dependent structural diversities of the inner carbon cores as well as the outer functional groups provide CQDs with versatile physicochemical properties and functionalities.[33–41] In this regard, we put forward a nanocarbon-enabled hybridization strategy to realize the fusion of different but cooperative pharmacophoric moieties in a single nanoformulation *via* the synthetic principles of

[a]*State Key Laboratory of Rare Earth Resources Utilization and Laboratory of Chemical Biology, Changchun Institute of Applied Chemistry, Chinese Academy of Sciences, Changchun, Jilin 130022, P. R. China. E-mail: jren@ciac.ac.cn; xqu@ciac.ac.cn*

[b]*Jilin Provincial Key Laboratory of Tooth Development and Bone Remodeling, Hospital of Stomatology, Jilin University, Changchun, Jilin 130021, P. R. China*

[c]*State Key Laboratory of Powder Metallurgy, Central South University, Changsha, Hunan 410083, P. R. China*

† Electronic supplementary information (ESI) available. See DOI: https://doi.org/10.1039/d4sc05280c

CQDs. In such a strategy, both the outer functional groups and the inner carbon cores in the nanoformulation can elicit desired pharmacological activities *via* rationally selecting precursors with appropriate bioactive moieties and polymerizable moieties, addressing the problems in both nanomedicine and medicinal chemistry to construct pharmacologically cooperative nanodrugs from small molecule drugs for remarkably enhanced efficacy.

As a proof-of-concept, the xCT antioxidant mechanism is selected herein as the therapeutic target to cooperatively enhance the efficacy of sonosensitizer-mediated sonodynamic therapy (SDT) of cancer. The xCT antioxidant mechanism is commonly elevated in cancer cells to confer resistance to therapeutics that rely on the generation of reactive oxygen species (ROS).[42–45] Notably, the efficacies of xCT pharmacological inhibitors and common sonosensitizers are generally hindered by the shortcomings such as small molecule drugs and insufficient sonocatalytic activity.[46–48] To achieve efficacious cooperativity, the xCT pharmacological inhibitor sulfasalazine is selected to hybridize with a co-nucleation precursor following our nanocarbon-enabled hybridization strategy to construct a pharmacologically cooperative CQD nanodrug (SCACDs) for ultrasound (US)-activated cancer therapy (Fig. 1a and b). Such a strategy endows SCACDs with dual enhanced pharmacological activities, which not only are 2–5 times superior to the classical nanoscale sonosensitizer TiO_2 in sonocatalytic generation of ROS owing to the appropriate band structure of the pharmacophoric carbon cores, but also show more than an order of magnitude higher antioxidant defense inhibitory activity than sulfasalazine *via* the transfer of the bioactive pharmacophores to the nanoscale. Through the pharmacological fusion at the nanoscale, SCACDs demonstrate a long body retention and favorable biodistribution and thus elicit dramatically enhanced anticancer efficacy at a very low injection dose *in vivo*.

Results and discussion

The SCACDs were synthesized *via* an alkali-assisted carbonization approach by using the xCT pharmacological inhibitor sulfasalazine as the pharmacophoric precursor, and citric acid as the co-nucleation precursor for promoting the carbonization and aromatization of the carbon cores. Such a carbonization process converted the orange-colored sulfasalazine and white-colored citric acid into the brown-colored SCACD product as indicated in Fig. S1.† The morphologies of the SCACDs were investigated by transmission electron microscopy (TEM) imaging. As shown in Fig. 1c, these SCACDs were extremely homogeneous with an average size of 2.44 nm (Fig. S2†). Fourier transform infrared spectroscopy (FT-IR) indicated the formation of the graphitic carbon cores in SCACDs, which showed the typical characteristic bands of the graphitic structure derived from citric acid (Fig. 2a). The powder X-ray diffraction (PXRD) pattern of SCACDs as indicated in Fig. 2b showed the characteristic diffractions of graphitic carbon.[31] Indeed, the Raman spectrum of SCACDs consisted of the D band and the G band, further indicating the formation of the graphitic carbon cores (Fig. 2c).[33] In addition, compared with the precursors sulfasalazine and citric acid, the significant changes in the results of thermogravimetric analysis (TGA) and derivative thermogravimetric analysis (DTG) indicated the newly formed SCACDs (Fig. 2d and S3†). The functional groups on SCACDs were then investigated by X-ray photoelectron spectroscopy (XPS) in detail. As shown in Fig. 2e, in the regions of C 1s, a sharp drop in the intensity of the peak centered at ~289.15 eV for the carboxyl groups in citric acid could be observed in the spectrum of SCACDs, indicating that citric acid was involved in the processes of polymerization, carbonization, and aromatization during the formation of the carbon cores. Moreover, the C-containing species of precursor sulfasalazine seemed to be preserved in SCACDs. In the regions of N 1s and S 2p, similar binding energy positions could be observed in the spectra of sulfasalazine and SCACDs, suggesting that the N- and S-containing species of the precursor sulfasalazine were preserved in SCACDs (Fig. 2f and g). In the region of O 1s as shown in Fig. 2h, the decreased intensity of the peak centered at ~532.80 eV for the oxygenated groups in citric acid also could be observed in the spectrum of SCACDs, further indicating the occurrence of carbonization. Additionally, the increased intensity of the O 1s peak centered at higher binding energies in the spectrum of SCACDs compared with that of the sulfasalazine and citric acid could be assigned to the adsorbed H_2O. Moreover, the distribution of the molecular weight of SCACDs is in *ca.* 1300–5000 as determined by matrix-assisted laser desorption/ionization time-of-flight mass spectrometry (MALDI-TOF MS) in Fig. 2i. Similar to other CQD nanostructures, these SCACDs exhibited photoluminescence (PL) properties with PL excitation (PLE) and PL peaks at 312 nm and 421 nm, respectively (Fig. 2j and k).

To deeply understand the structure of SCACDs, density functional theory (DFT) calculations were performed. Fig. 3a shows the model containing a sulfasalazine molecule and citric acid molecules. The simulation is under 473 K in accordance with the experimental carbonization process. Due to the large Gaussian height with 0.3 hartree at every 40 steps in this simulation, the reaction occurs at 1120 fs and Fig. 3b shows the state at 1680 fs. In Fig. 3b, one citric acid molecule moves close to the sulfasalazine molecule forming a carbon nucleus, and meanwhile, the pyridine group and the phenol group leave the fractured sulfasalazine molecule. However, such a carbon core is smaller than the critical size so that this structure collapses at 2000 fs as presented in Fig. 3c. However, this carbonization process doesn't always occur if we change the original arrangement of these molecules under 473 K. Also, considering the large Gaussian height for observing carbonization efficiently, it could be concluded that many sulfasalazine molecules left after the carbonization reaction. Hence, the main carbon cores originated from citric acid as the template. A small amount of sulfasalazine molecules is decomposed. Then the connection between these fractured groups and the carbon core is simulated at stage 2. At stage 2, the SPRINT as the collective variable is selected to simulate the formation of the carbon core from the nucleus. Four nuclei from Fig. 3b are set close to obtain a larger carbon core during the simulation. Meanwhile, the two fractured groups also exist in this model so that we

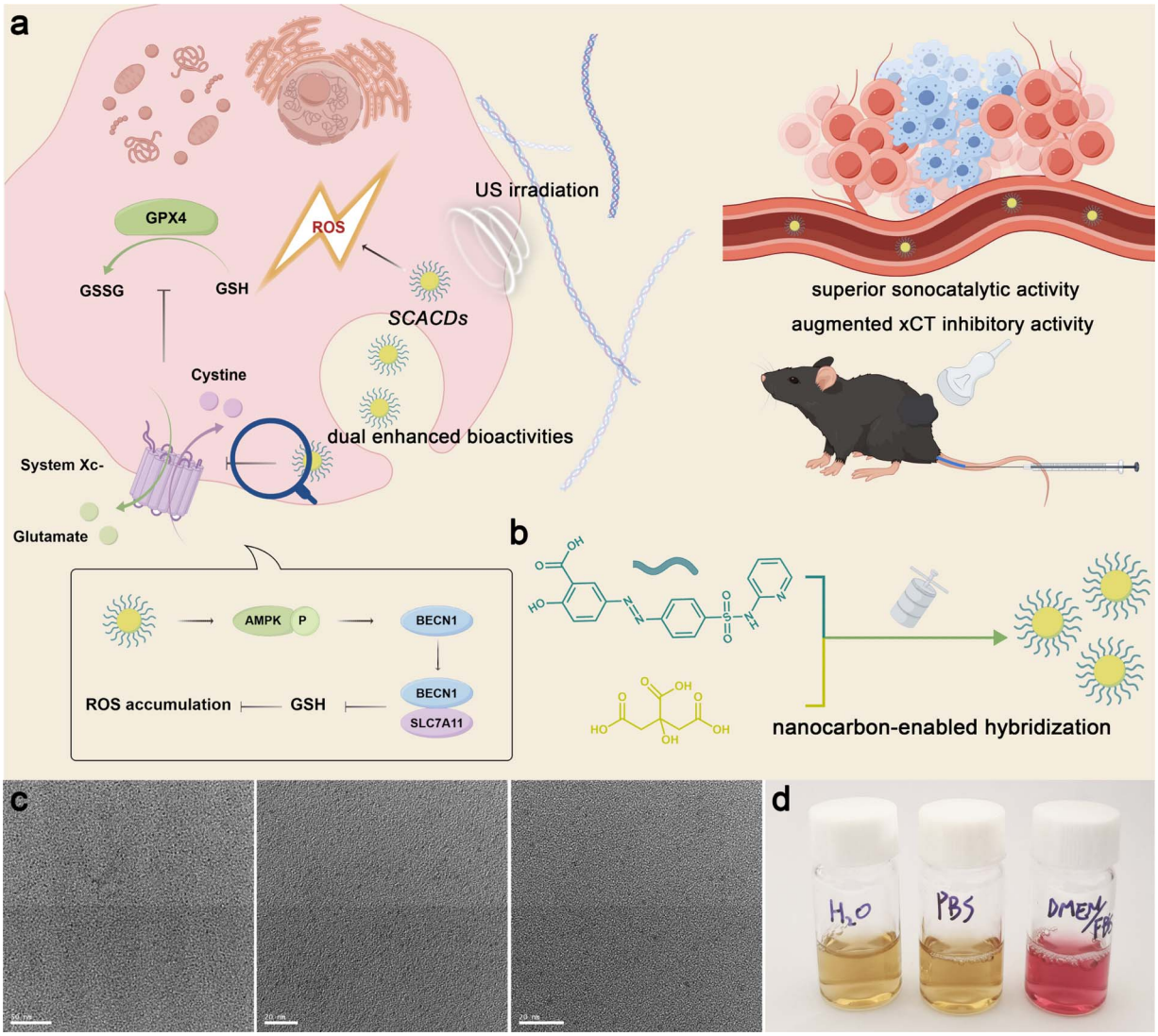

Fig. 1 Characterization and properties of SCACDs. (a) Schematic illustration of the construction of SCACDs with dual enhanced bioactivities *via* the nanocarbon-enabled hybridization strategy for reinforced melanoma therapy. Created with Figdraw. For *in vitro* and *in vivo* applications, SCACDs are functionalized with PEG. The PEG component is not shown in (a) to highlight the structure of the surface pharmacophores. (b) Sulfasalazine is selected to hybridize with citric acid following the present strategy to construct a pharmacologically cooperative nanodrug. Created with Figdraw. (c) TEM images of SCACDs. Scale bars are equal to 50 nm, 20 nm, and 20 nm from left to right. (d) Digital images of SCACDs dispersed in water, PBS, and DMEM containing 10% FBS.

attempt to understand how these fracture groups and the whole sulfasalazine molecule are connected to the carbon cores. All these simulation processes listed in Fig. 3d–f indicate that the final structure of the carbon core is the nitrogen-doped carbon core with a graphitic structure. The phenol group-containing benzene ring loses an H atom to incorporate into the carbon core, but the pyridine group is only adsorbed by the carbon core. This result demonstrates that the connection in the sequence of pyridine-N-S-carbon core does not exist. These two fractured groups can only be incorporated into the carbon core or washed away. So, based on the simulation we give a hypothetical structure of the final SCACDs presented in Fig. 3g which is subjected to geometric optimization using Gaussian 16 software. The O atoms on the hydroxy and carboxyl groups of the precursor sulfasalazine connect to the exposed carbon on the carbon core after losing H atoms in alkaline aqueous solution. Otherwise, the un-protonated sulfasalazine molecules are only adsorbed by the carbon core in terms of our molecular dynamics simulation. In conclusion, our two-step simulations indicate that the carbon cores originate from citric acid mainly, and few sulfasalazine molecules are carbonized which combined with the citric acid molecules. Some fractured sulfasalazine molecules provide the N element to the carbon cores. The majority of sulfasalazine molecules are deprotonated in the alkaline solution connecting to the nitrogen-doped carbon cores during the carbonization process. As the real carbon core is larger than the carbon core presented in Fig. 3g, this smaller

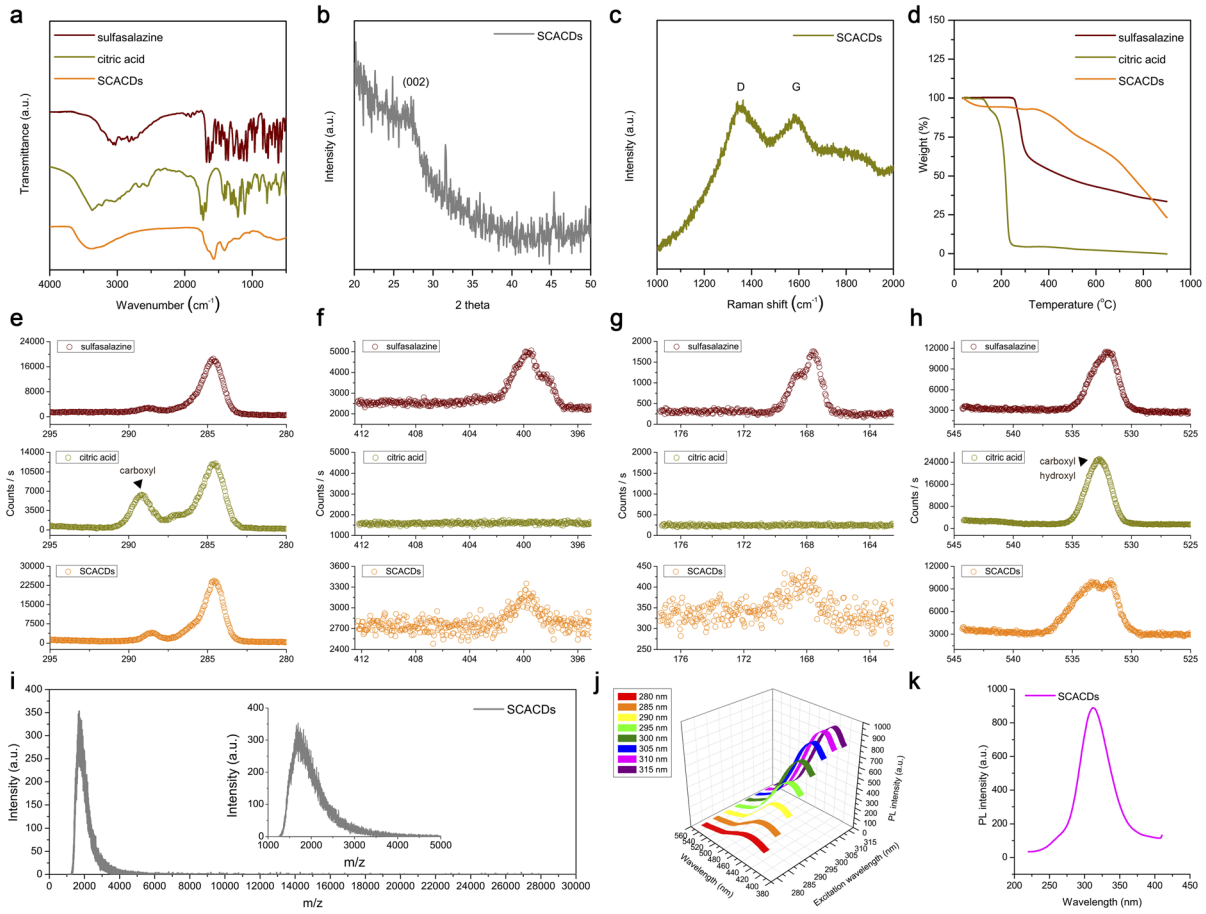

Fig. 2 Characterization of SCACDs. (a) FT-IR spectra of the precursor sulfasalazine and the co-nucleation precursor citric acid, as well as the SCACDs. PXRD pattern (b) and Raman spectrum (c) of SCACDs. (d) TGA curves of the precursor sulfasalazine and the co-nucleation precursor citric acid, as well as the SCACDs. High-resolution C 1s (e), N 1s (f), S 2p (g), and O 1s (h) XPS spectra of the precursor sulfasalazine and the co-nucleation precursor citric acid, as well as the SCACDs. (i) MALDI-TOF MS spectrum of SCACDs. (j) PL spectra of SCACDs under different excitations. (k) PLE spectrum of SCACDs. Emissions: 421 nm.

model is aimed for the following ^{13}C NMR and the time-dependent DFT (TDDFT) calculations.

Table S1 and Fig. S5† indicate the calculated nuclear magnetic resonance spectra (NMR) of sulfasalazine molecules with different functionals in comparison with the experimental NMR results characterized by cross polarization/magic angle spinning (CP/MAS) ^{13}C NMR spectroscopy. Also, the average results from our three supposed models by Boltzmann thermal distribution are listed in Table S1.† Although the structures of the sulfasalazine molecule are not only these three types, however, the real calculated average values are not the goal of the present study. Hence, the above three types of sulfasalazine molecules are considered to prove the correction of our NMR calculation. The key is the NMR of SCACDs in accordance with the calculated result based on our hypothetical structure. Considering the common error of this kind calculation, the revTPSS functional is better so that the NMR calculation of final SCACDs using the revTPSS functional is presented in Fig. 3g. The peak below 70 ppm represents the hydrocarbon branches on the carbon core which exist in the simulation in Fig. 3f. And the peak around 180 ppm mainly originates from the aldehyde group on the carbon core instead of carboxyl or ketone with about 200 ppm according to the calculations. The good fitness between calculation and experiment results indicates the correction of our hypothesis. The absorption spectrum obtained by the TDDFT method is presented in Fig. 3h for comparison with experimental results to confirm our hypothesis. To avoid the influence of sulfasalazine, the pure nitrogen-doped carbon core is used in this calculation, as the real carbon cores are much larger than this model in Fig. 3g. Therefore, the main absorption is provided by the carbon cores rather than sulfasalazine. The differences of absorption spectra between the pure nitrogen-doped carbon core and the sulfasalazine indicates the carbon core mainly existence after the carbonization reaction in accordance with our experimental result. All these theoretical results indicated that the hybridized SCACDs possessed a hybridized nanostructure, realizing the pharmacological fusion of the pharmacophoric nitrogen-doped carbon cores as the sonocatalytic component and the connected pharmacophoric moiety of sulfasalazine as the cooperative xCT inactivating component. The elemental analysis indicated that the contents of C, N, and S were 37.15%, 6.07%, and 0.84%,

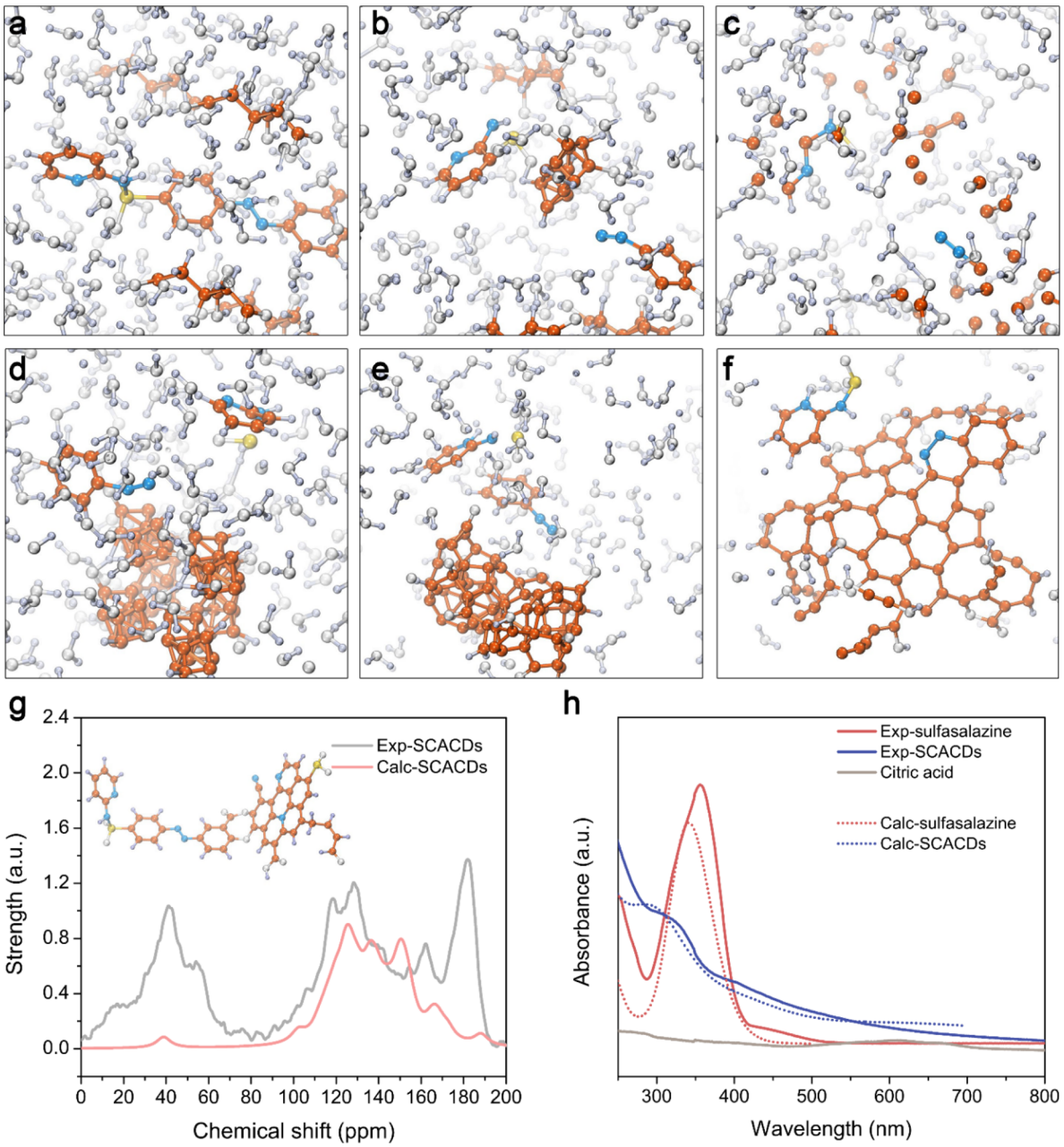

Fig. 3 DFT calculations. The metadynamics simulation of the nucleation process of a sulfasalazine molecule and citric molecules in water. (a–c) Stage 1. (d–f) Stage 2. The orange, blue, yellow, white, and light purple represent C, N, S, O, and H, respectively. (a) The beginning state. (b) Nucleation state at 1680 fs. (c) Devastation at 2000 fs. (d) The beginning of stage 2. (e) The larger nucleus formed. (f) The nitrogen-doped carbon core formed with the unbonded fractured group after 220 ps. (g) The calculated NMR spectrum compared with the experimental NMR spectrum of SCACDs. (Inset) The hypothetical final structure of SCACDs after the hydrothermal reaction. (h) The calculated UV-Vis spectra of sulfasalazine and the nitrogen-doped carbon core in SCACDs compared with the experimental UV-Vis spectra of sulfasalazine and the SCACDs.

respectively. Based on the S content in sulfasalazine as the reference, the pharmacophoric element of sulfasalazine in SCACDs could be estimated at ~10.6%. Additionally, SCACDs showed high stability in water even after being stored for 6 months as indicated by NMR and UV-Vis spectra in Fig. S6.†

The sonocatalytic activity of SCACDs for ROS production was then explored in detail *via* electron spin resonance (ESR) spectroscopy with spin trapping, which is the most reliable and direct method for identification and quantification of short-lived ROS. By using DMPO and TEMP as the spin probes, dramatically increased ESR signal intensities for the DMPO/$^{\bullet}O_2^-$ spin adduct as well as the TEMP/$^1O_2$ spin adduct could be observed in the presence of SCACDs under US irradiation, indicating the efficient sonocatalytic generation of superoxide anion radicals ($^{\bullet}O_2^-$) and singlet oxygen ($^1O_2$). Fig. 4a–d indicate that the sonocatalytic generation of $^{\bullet}O_2^-$ and $^1O_2$ by SCACDs was concentration-dependent and time-dependent. In contrast, a negligible ESR signal could be detected in the samples

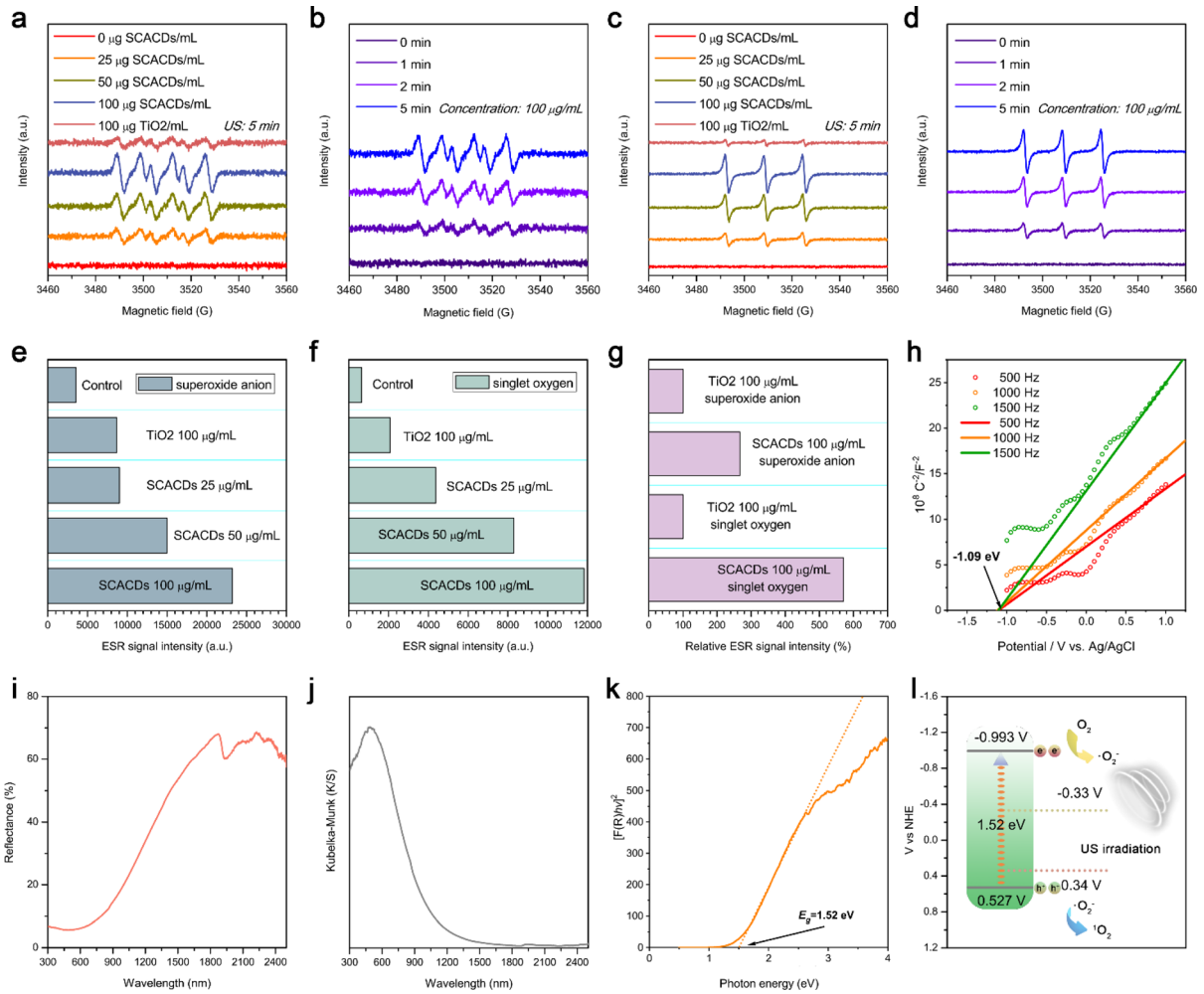

Fig. 4 Sonocatalytic generation of ROS *via* SCACDs. Concentration-dependent (a) and time-dependent (b) generation of $^{\bullet}O_2^-$ of SCACDs under US irradiation (1.0 MHz, 0.5 W cm^{-2}) as demonstrated by ESR spectra. Concentration-dependent (c) and time-dependent (d) generation of $^1O_2$ of SCACDs under US irradiation (1.0 MHz, 0.5 W cm^{-2}) as demonstrated by ESR spectra. DMPO and TEMP and DMPO are used as the trapping agents to investigate the generation of $^{\bullet}O_2^-$ and $^1O_2$, respectively. For concentration-dependent experiments, the US irradiation period is 5 min. For time-dependent experiments, the concentration of SCACDs is 100 μg mL^{-1}. (e) The $^{\bullet}O_2^-$ generating abilities of SCACDs and TiO_2 quantified using the ESR signal intensities. (f) The $^1O_2$ generating abilities of SCACDs and TiO_2 quantified using the ESR signal intensities. (g) Relative ESR signal intensities for the SCACD sample in the presence of the spin probe TEMP or DMPO under US irradiation. The TiO_2 sample containing the spin probe TEMP or DMPO under US irradiation is used as the control sample under the same experimental conditions. (h) Mott–Schottky plots for SCACDs in 0.5 M Na_2SO_4 aqueous solution at frequencies of 500 Hz, 1000 Hz, and 1500 Hz. (i) UV-Vis-DRS spectrum of SCACDs. (j) The absorption spectrum of SCACDs transformed from the UV-Vis-DRS spectrum by using the Kubelka–Munk function. (k) Tauc plots for SCACDs. (l) Schematic diagram of the band structure of SCACDs for sonocatalytic generation of $^{\bullet}O_2^-$ and $^1O_2$.

containing SCACDs and the corresponding spin probes without US irradiation or in the samples containing the corresponding spin probes alone with US irradiation. The classical sensitizer P25 TiO_2 was then used for comparison to explore the sonocatalytic efficacy of the SCACDs. Surprisingly, the sonocatalytic efficacies for the generation of $^{\bullet}O_2^-$ and $^1O_2$ by SCACDs were much higher compared with those of P25 TiO_2 under the same experimental conditions (Fig. 4e–g). To understand the high ROS-generating ability of SCACDs, the band structure was evaluated using the Mott–Schottky plot and UV-Vis diffuse reflectance spectrum (UV-Vis-DRS). As shown in Fig. 4h, the positive slopes of the Mott–Schottky plots at frequencies of 500 Hz, 1000 Hz, and 1500 Hz were consistent with that of typical n-type semiconductors. Moreover, the flat band potential (E_{fb}) determined from the intersection is approximately −1.09 V *versus* Ag/AgCl (−0.893 V *versus* NHE). Generally, the E_{fb} determined by the Mott–Schottky method is higher than the conduction band (CB) position by about 0.1 V. Hence, the CB of SCACDs could be estimated to be −0.993 V *versus* NHE. Moreover, UV-Vis-DRS and the corresponding Kubelka–Munk function-transformed absorption spectrum of SCACDs were recorded as indicated in Fig. 4i and j. The Tauc plot results as shown in Fig. 4k indicated that the bandgap energy of SCACDs was approximately 1.52 eV; thus the valence band (VB) of SCACDs could be calculated to be 0.527 V *versus* NHE. With a more negative potential of the CB in SCACDs than the

reduction potential of $O_2/^{\bullet}O_2^-$ (−0.33 V *versus* NHE) and a more positive potential of the VB in SCACDs than the oxidation potential of $^{\bullet}O_2^-/^1O_2$ (0.34 V *versus* NHE), the sonocatalytic generation of ROS over SCACDs is feasible (Fig. 4l).[49,50] A narrow bandgap can result in a high sonodynamic activity *via* facilitating the US-mediated production of electron–hole pairs for subsequently activating the surrounding substrates to generate ROS.[37] Compared with P25 TiO_2, the significantly narrower bandgap of SCACDs could obviously improve the sonocatalytic efficacy (Fig. S7†). Moreover, the distance between the CB of SCACDs and the redox potential of $O_2/^{\bullet}O_2^-$ is farther than that of P25 TiO_2, whereas the distance between the VB of SCACDs and the redox potential of $^{\bullet}O_2^-/^1O_2$ is much closer than that of P25 TiO_2 (Fig. S8†). As a closer distance can facilitate the reactions of electrons/holes with substrates to generate ROS, SCACDs were more effective in sonocatalytic generation of $^1O_2$ than $^{\bullet}O_2^-$. Quantitatively, compared with P25 TiO_2, the ESR signal intensities of the DMPO–OOH or TEMPO increased by 266.9% and 570.4% under the same experimental conditions, demonstrating that SCACDs were 2–5 times superior to P25 TiO_2 in sonocatalytic generation of ROS (Fig. 4g). The above results collectively indicated the superior sonocatalytic activity of SCACDs for ROS generation under US irradiation, which arose from the appropriate band structure as well as the narrow bandgap of the pharmacophoric carbon cores in SCACDs.

For biological usages, SCACDs were further noncovalently functionalized with poly(ethylene glycol) (PEG) *via* the interaction between the graphitic carbon cores and terminal phospholipid groups of DSPE-mPEG to diminish the association with nontargeted serum and tissue proteins. As shown in Fig. S9–S11,† the ζ potential value of PEGylated SCACDs showed a slight increase compared with that of SCACDs, from -17.58 ± 0.63 mV to -7.85 ± 0.12 mV. The digital photograph in Fig. 1d demonstrated that PEGylated SCACDs exhibited high dispersibility in water, phosphate buffered saline (PBS), and Dulbecco's modified Eagle medium (DMEM) containing 10% fetal bovine serum (FBS). For convenience, the PEGylated SCACDs were also termed SCACDs in the following biological studies. Murine melanoma cells (B16F10) were thereafter selected as a typical cell line for subsequent *in vitro* studies to investigate the pharmacological activities of SCACDs. The high level of xCT developed by melanoma greatly strengthens the cellular antioxidant defense and thus confers resistance to ROS-mediated therapeutics.[42,45,51] Thus, the pharmacological activity of SCACDs for xCT antioxidant mechanism blockade was first explored. The transporter subunit xCT in system xc^- is responsible for the cellular cystine uptake to produce glutathione (GSH) and maintain the intracellular redox balance. The cellular cystine uptake of SCACD-treated melanoma cells was first investigated. Fig. 5a shows significantly decreased cystine uptake by melanoma cells after co-incubating with SCACDs, indicating the inactivation of the xCT antioxidant mechanism. With the same dose of the pharmacophoric element of sulfasalazine, SCACDs showed much higher activity in xCT inactivation than the small molecule sulfasalazine. The intracellular GSH level of SCACD-treated melanoma cells was explored. As demonstrated in Fig. 5b and c, SCACDs could effectively decrease the intracellular level of GSH, which could be also verified by flow cytometry (Fig. S12†). Quantitatively, compared with sulfasalazine, SCACDs could deplete intracellular GSH with 1520.01% efficacy with the same dose of the pharmacophoric element, indicating that SCACDs elicit more than an order of magnitude higher antioxidant defense inhibitory activity than the small molecule inhibitor (Fig. 5b). Indeed, significantly increased ROS levels could be observed in SCACD-treated B16F10 cells owing to the enhanced xCT inhibitory activity (Fig. 5d). These results demonstrated that SCACDs could greatly augment the pharmacological activity of sulfasalazine *in vitro*, which could be attributed to the effective cellular uptake of SCACDs. As shown in Fig. 5e, Cy5-labeled SCACDs (Cy5-SCACDs) could be well internalized by B16F10 cells in a time-dependent manner. It has been demonstrated that the xCT-mediated cystine uptake facilitates the intracellular biosynthesis of not only GSH, but also GPX4.[52,53] Indeed, as shown in Fig. 5f and g, SCACDs could effectively decrease the expression level of GPX4 in B16F10 cells. These results unambiguously indicated the xCT inactivating ability of SCACDs. Generally, xCT pharmacological inhibitors including sulfasalazine elicit their pharmacological activity by promoting the formation of the Beclin 1-SLC7A11 complex that is mediated by the activation of AMP-activated protein kinase (AMPK) as shown in Fig. 1a.[54] As shown in Fig. 5f, g and S15,† SCACDs could effectively activate AMPK and induce the conversion of the autophagic marker LC3B-I to LC3B-II. Meanwhile, the increased interaction between Beclin 1 and SLC7A11 after treating with SCACDs could be observed in the result of immunoprecipitation assay (Fig. 5h). Notably, SCACDs showed significantly more effective bioactivity than that of sulfasalazine with the same dose of the pharmacophoric element as indicated by the above western blot analysis and immunoprecipitation assay.

The sonodynamic anticancer efficacy was therefore investigated *in vitro*. B16F10 cells were randomly divided into six groups and defined as control, sulfasalazine alone, SCACDs alone, US alone, TiO_2 + US, and SCACDs + US, respectively. As displayed in Fig. 6a and b, an MTT assay associated with B16F10 cells without US irradiation demonstrated that the cellular viability was slightly hindered by SCACDs at relatively high concentrations. Upon US irradiation (1 MHz, 1 W cm^{-2}, 1 min), the treatment of SCACDs + US showed much higher *in vitro* anticancer activity compared with that in the groups of control, US, sulfasalazine, SCACDs, and TiO_2 + US, which could be attributed to the high US-triggered ROS-generating ability as well as the augmented xCT inhibitory activity of SCACDs (Fig. 6b). The cytotoxicity of SCACDs on normal cells was then evaluated by using HaCat cells (human epithelial cells) to investigate the biosafety of SCACDs for therapeutic uses. As shown in Fig. 6c and S16,† the cytotoxicity of SCACDs towards HaCat cells was lower than that towards B16F10 cells, which might be attributed to the fact that cancer cells have developed increased levels of xCT, making them much more sensitive to xCT antioxidant mechanism disturbance. Thus, SCACDs exhibited selective cytotoxicity towards melanoma cells. The *in vitro* ROS-generating activity of SCACDs was further investigated. As shown in Fig. 5d, the results of flow cytometry also

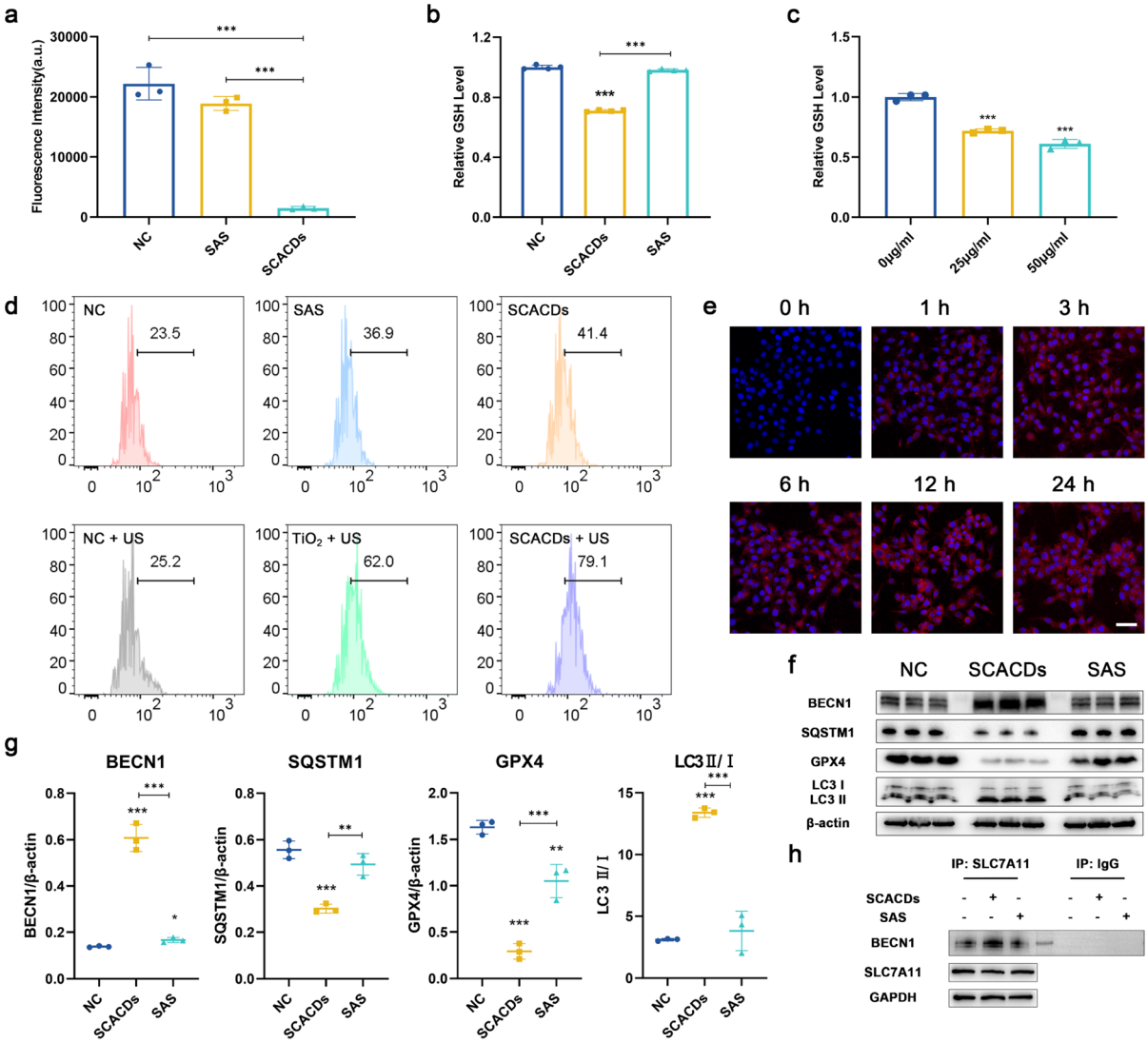

Fig. 5 *In vitro* pharmacological activity of SCACDs. (a) The relative cystine uptake by B16F10 cells after incubating with SCACDs (25 μg mL^{-1}) or sulfasalazine (SAS) with the same dose of the pharmacophoric element as determined by the cystine uptake assay kit. Error bars represent standard deviation from the mean ($n = 3$). (b) Quantitative analysis of GSH levels in B16F10 cells after incubating with SCACDs (25 μg mL^{-1}) or SAS with the same dose of the pharmacophoric element. Error bars represent standard deviation from the mean ($n = 4$). (c) Quantitative analysis of GSH levels in B16F10 cells after incubating with different concentrations of SCACDs. Error bars represent standard deviation from the mean ($n = 3$). (d) Flow cytometry analysis of US-triggered ROS generation in B16F10 cells after various treatments. US parameters: 1.0 MHz, 1 W cm^{-2}, 1 min. (e) Time-dependent cellular uptake of Cy5-SCACDs. The scale bar is equal to 50 mm. (f and g) Western blot analysis of B16F10 cells after various treatments and related quantitative analysis data. Error bars represent standard deviation from the mean ($n = 3$). (h) Immunoprecipitation assay indicates the increased interactions between Beclin 1 and SLC7A11 in B16F10 cells after SCACD treatment. Asterisks indicate statistically significant differences (*$P < 0.05$, **$P < 0.01$, and ***$P < 0.001$). The group of NC indicates the negative control group.

verified the ROS-mediated anticancer activity of SCACDs *in vitro* under US irradiation. The anti-proliferative effect of SCACDs was further investigated by a cell colony formation assay. As shown in Fig. 6d, B16F10 cells in the group of SCACDs + US revealed much fewer colonies compared with those in the groups of control, US, sulfasalazine, SCACDs, and TiO_2 + US, indicating the high US-triggered anti-proliferative ability of SCACDs. The US-triggered cell-killing activity of SCACDs was further demonstrated by Annexin V-FITC/PI apoptosis detection (Fig. 6e). Besides, the expressions of apoptosis biomarkers including caspase 3 and PARP in SCACDs-treated B16F10 cells upon US irradiation were further investigated by western blot analysis. Indeed, B16F10 cells were killed by SCACDs through an apoptosis process (Fig. 6f). Taken together, the SCACDs with ultrahigh sonocatalytic activity and significantly augmented xCT inhibitory activity exhibited cooperatively enhanced anticancer efficacy *in vitro*.

We then investigated the biocompatibility of SCACDs prior to exploring the *in vivo* anticancer efficacy. The results of hemolytic assay in Fig. S18† demonstrate that no obvious hemolysis was detected after co-incubating with SCACDs. Then, male C57BL/6 mice were used to investigate the *in vivo*

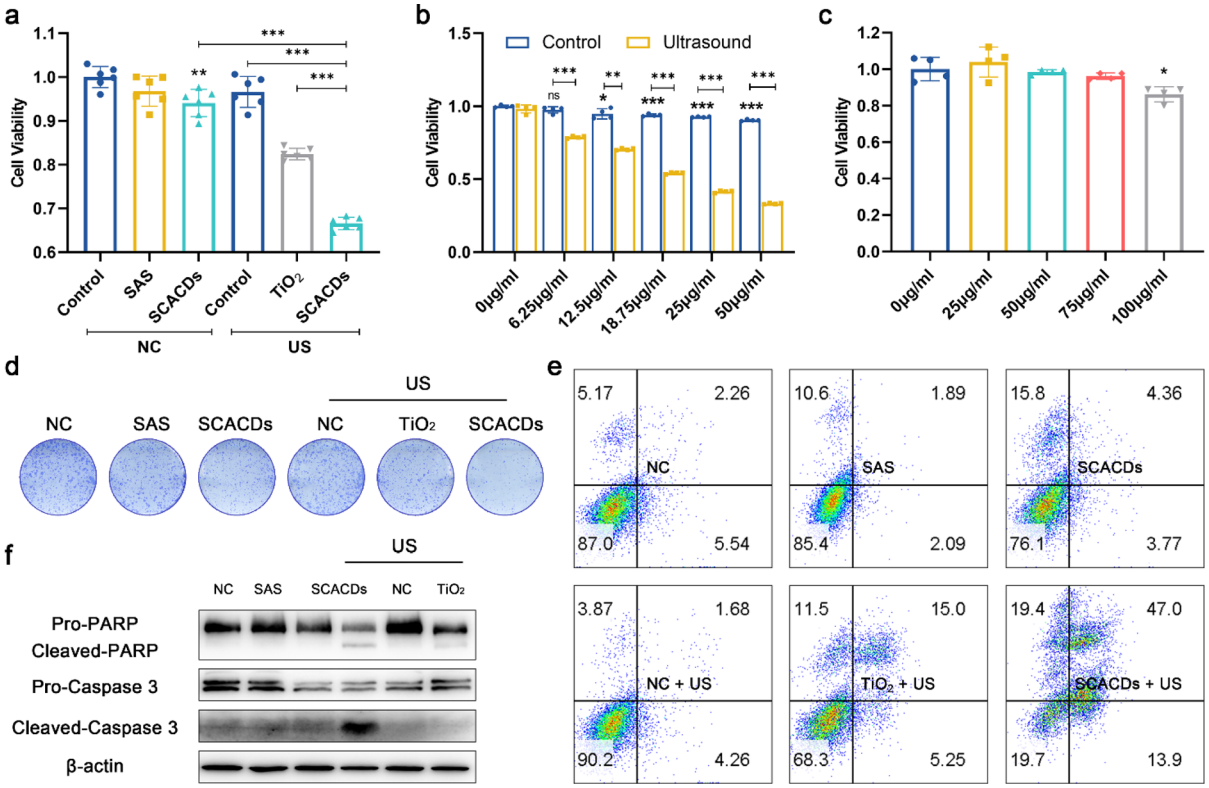

Fig. 6 *In vitro* anticancer efficacy. (a) Viability of B16F10 cells after various treatments. Error bars represent standard deviation from the mean ($n = 6$). (b) Cytotoxicity and SDT efficacy of SCACDs. US parameters: 1.0 MHz, 1 W cm^{-2}, 1 min. Error bars represent standard deviation from the mean ($n = 4$). (c) Viability of HaCaT cells after incubating with various concentrations of SCACDs for 1 day. Error bars represent standard deviation from the mean ($n = 4$). (d) Representative digital photographs of the colony formation assay of B16F10 cells after various treatments. (e) Apoptosis/necrosis analysis of B16F10 cells after various treatments based on flow cytometry. (f) Western blot analysis of B16F10 cells after various treatments. Asterisks indicate statistically significant differences (*$P < 0.05$, **$P < 0.01$, and ***$P < 0.001$). The group of NC indicates the negative control group.

biocompatibility of SCACDs (24 mg kg^{-1}). Compared with the mice in the control group, mice intravenously injected with SCACDs showed negligible differences in bodyweight (Fig. S19†). Hematoxylin and eosin (H&E) staining images of major organs including the heart, liver, spleen, lung, and kidney as well as the results of blood biochemistry and hematology demonstrated the overall biosafety of SCACDs (Fig. S20–S22†). These results collectively revealed the high biocompatibility of SCACDs and their high potential for melanoma therapy. The biodistribution of these SCACDs in B16F10 tumor-bearing mice was further investigated by using Cy5-SCACDs. Time-dependent *ex vivo* fluorescence imaging was thus carried out to record the biodistribution of Cy5-SCACDs in major organs and tumors visually. As expected, the fluorescence signals from Cy5-SCACDs could be detected in the tumors from 24 h to 72 h post-injection, indicating the long body retention and effective tumor accumulation of SCACDs *in vivo* (Fig. S23†). Notably, the fluorescence signals from Cy5-SCACDs in the tumors could be partially shielded by the black melanoma tissues. Additionally, most of the Cy5-SCACDs accumulated in the kidneys during the experimental period of 72 h, and the fluorescence signals from Cy5-SCACDs in other organs decreased over time, demonstrating the renal clearance characteristics of SCACDs.

The *in vivo* anticancer efficacy of SCACDs was then investigated in detail. C57BL/6 mice bearing B16F10 tumors were randomly divided into five groups and defined as control, US, sulfasalazine (6 mg kg^{-1}), SCACDs (6 mg kg^{-1}), and SCACDs (6 mg kg^{-1}) + US. At 12 h, 36 h, and 60 h after intravenous injection of SCACDs, the tumors received US irradiation (1 MHz, 2 W cm^{-2}, 3 min). The mice were intravenously injected with SCACDs or sulfasalazine every three days. Tumor volumes were recorded to investigate the anticancer efficacy of SCACDs *in vivo* (Fig. 7a). The tumor volumes of mice in the group of SCACDs were obviously smaller than those in the control group and the group of sulfasalazine, indicating that SCACDs could greatly augment the bioactivity and enhance the tumor retention and accumulation of the pharmacophoric element of sulfasalazine. It is noteworthy that the injection dose of sulfasalazine was nearly 10 times higher than that of the pharmacophoric element of sulfasalazine in the SCACDs. Indeed, the augmented xCT inhibitory activity of SCACDs could be re-verified by GPX4 and GSH staining immunofluorescence images of tumor slices (Fig. S24†). Upon US irradiation, SCACD-mediated sonocatalytic ROS production greatly enhanced the anticancer effects, and complete tumor elimination could be observed in the group of SCACDs + US with no tumor relapse. Notably, the dose of

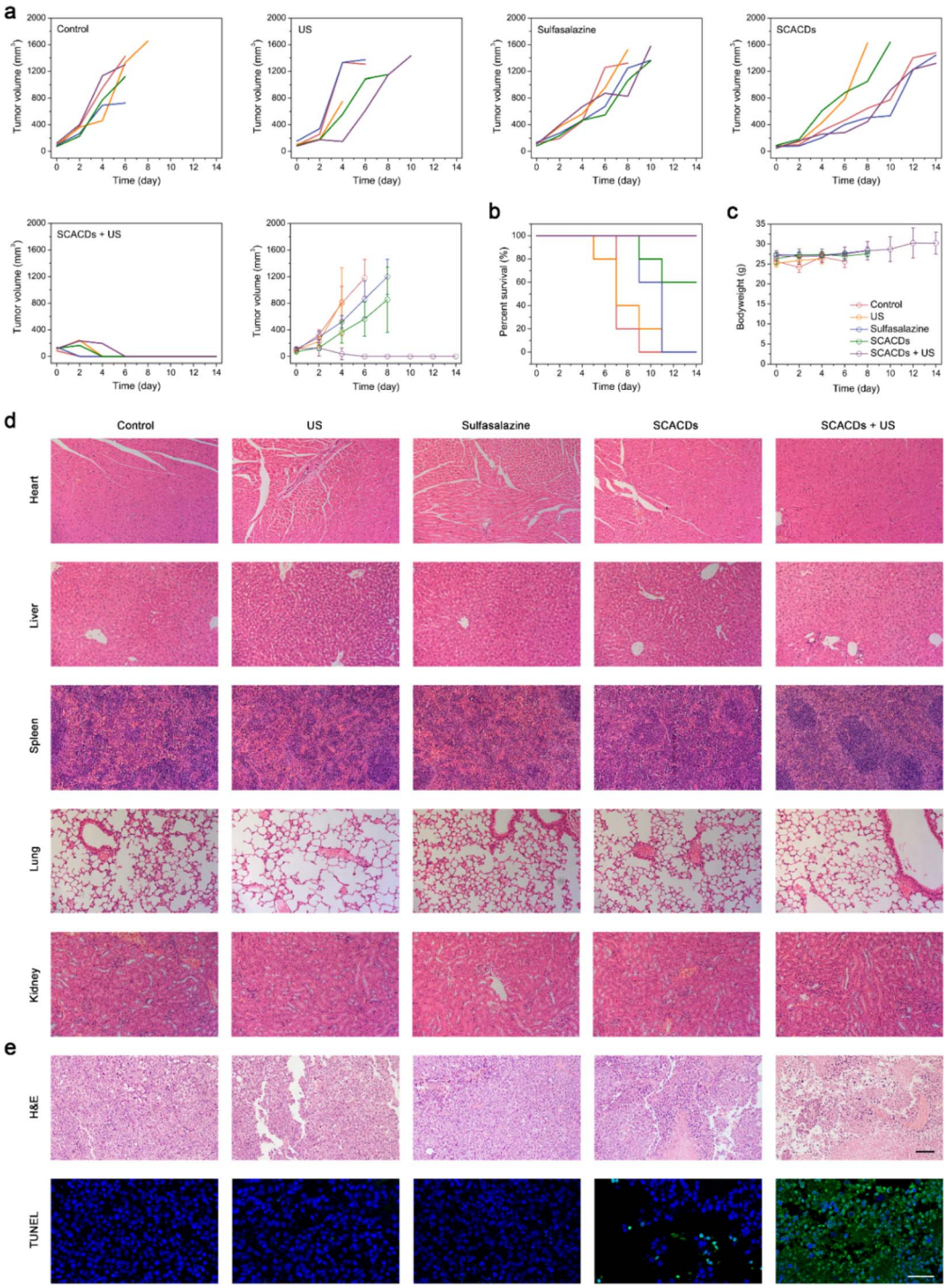

Fig. 7 *In vivo* anticancer efficacy of SCACDs. (a) Tumor growth curves of the B16F10 tumor-bearing mice after various treatments. (b) Survival curves of the B16F10 tumor-bearing mice after various treatments. (c) Bodyweight changes of the B16F10 tumor-bearing mice after various treatments. (d) H&E-stained images of the slices of the major organs collected from various experimental groups. (e) H&E-stained images of the slices of the tumors collected from various experimental groups. The scale bar is equal to 100 μm. TUNEL-stained images of the slices of the tumors collected from various experimental groups. The scale bar is equal to 50 μm. Error bars represent standard deviation from the mean (n = 5).

SCACDs required for SDT (6 mg kg^{-1}) was very low, which was 4 times lower than that used in the biosafety studies (24 mg kg^{-1}). To deeply understand the anticancer efficacy of SCACDs, hematoxylin and eosin (H&E) staining and terminal deoxynucleotidyl transferase-mediated dUTP nick-end labeling (TUNEL) staining were further performed. As shown in Fig. 7e, the group of SCACDs + US exhibited a high level of melanoma cell apoptosis. Moreover, the survival curves of mice in various

groups were also recorded, suggesting that SCACDs were highly efficient for melanoma therapy (Fig. 7b). In addition, mice in all groups exhibited no obvious differences in body weight during the whole experimental period as indicated in Fig. 7c, and H&E staining images of major organs from mice in various groups revealed the high biocompatibility of SCACDs (Fig. 7d). All the above results indicated that SCACDs could act as high-performance anticancer nanodrugs *in vivo*, showing dramatically enhanced therapeutic efficacy *via* the pharmacological fusion at the nanoscale through our nanocarbon-enabled hybridization strategy.

Conclusions

In summary, based on the principles of pharmacophore hybridization in medicinal chemistry and CQD synthesis in nanotechnology, the nanocarbon-enabled hybridization strategy proposed in the present study aimed to construct pharmacologically cooperative nanodrugs for greatly reinforced anticancer therapeutics. The SCACDs are composed of inner carbon cores with an appropriate band structure for highly effective US-triggered ROS generation and outer bioactive pharmacophores with obviously augmented bioactivity for antioxidant defense inhibition in cancer cells, realizing remarkably improved US-activated cancer cell-killing activity. Significantly, SCACDs inherit the advantages of CQDs including high stability, long body retention, and favorable biodistribution, providing them with high *in vivo* anticancer efficacy and biocompatibility that are conducive to their further clinical translation. Overall, the proof-of-concept construction of SCACDs *via* the nanocarbon-enabled hybridization strategy offers a facile yet effective approach toward pharmacologically cooperative nanodrugs with remarkably augmented therapeutic efficacy.

Data availability

The data supporting this article have been included as part of the ESI.†

Author contributions

H. W., J. R., and X. Q. conceived and designed the study. H. W. performed the synthesis of the materials. H. W. and X. Y. performed the characterization of the materials. H. W., X. Y., and Y. D. performed the theoretical studies. X. L. performed the cell culture studies. H. W. performed the confocal imaging as well as the *ex vivo* imaging experiments. H. W. and X. L. performed the biosafety studies. H. W. and X. L. assisted with *in vivo* studies. H. W., X. L., X. Y., F. P., and J. R. analyzed the experimental data and wrote the paper. All the authors discussed the results and commented on the manuscript. J. R. and X. Q. supervised the whole project.

Conflicts of interest

There are no conflicts to declare.

Acknowledgements

This work was supported by the Science and Technology Development Project of Jilin Province (20230101040JC), the National Key R&D Program of China (2022YFA1205804 and 2021YFF1200700), and the National Natural Science Foundation of China (22475210, 22437006, 22105197, and 22237006). This work was supported in part by the High-Performance Computing Center of Central South University. The ESR spectra, UV-Vis-DRS spectra, and the Mott–Schottky plots were obtained with the assistance of the JDHR Lab. Schematics in Fig. 1 were created using Figdraw (**https://www.figdraw.com/**) and used with permission.

Notes and references

1 V.-J. Claudio, D. Amanda, B. Vanderlan da Silva, J. B. Eliezer and F. Carlos Alberto Manssour, Molecular Hybridization: A Useful Tool in the Design of New Drug Prototypes, *Curr. Med. Chem.*, 2007, **14**, 1829–1852.
2 B. Meunier, Hybrid Molecules with a Dual Mode of Action: Dream or Reality?, *Acc. Chem. Res.*, 2008, **41**, 69–77.
3 M. Grigalunas, S. Brakmann and H. Waldmann, Chemical Evolution of Natural Product Structure, *J. Am. Chem. Soc.*, 2022, **144**, 3314–3329.
4 J. Noh, B. Kwon, E. Han, M. Park, W. Yang, W. Cho, W. Yoo, G. Khang and D. Lee, Amplification of oxidative stress by a dual stimuli-responsive hybrid drug enhances cancer cell death, *Nat. Commun.*, 2015, **6**, 6907.
5 D. Mao, S. Ando, S.-i. Sato, Y. Qin, N. Hirata, Y. Katsuda, E. Kawase, T.-F. Kuo, I. Minami, Y. Shiba, K. Ueda, N. Nakatsuji and M. Uesugi, A Synthetic Hybrid Molecule for the Selective Removal of Human Pluripotent Stem Cells from Cell Mixtures, *Angew. Chem., Int. Ed.*, 2017, **56**, 1765–1770.
6 Y. Luan, J. Li, J. A. Bernatchez and R. Li, Kinase and Histone Deacetylase Hybrid Inhibitors for Cancer Therapy, *J. Med. Chem.*, 2019, **62**, 3171–3183.
7 A. Çapcı, M. M. Lorion, H. Wang, N. Simon, M. Leidenberger, M. C. Borges Silva, D. R. M. Moreira, Y. Zhu, Y. Meng, J. Y. Chen, Y. M. Lee, O. Friedrich, B. Kappes, J. Wang, L. Ackermann and S. B. Tsogoeva, Artemisinin–(Iso) quinoline Hybrids by C−H Activation and Click Chemistry: Combating Multidrug-Resistant Malaria, *Angew. Chem., Int. Ed.*, 2019, **58**, 13066–13079.
8 M. Tyers and G. D. Wright, Drug combinations: a strategy to extend the life of antibiotics in the 21st century, *Nat. Rev. Microbiol.*, 2019, **17**, 141–155.
9 R. A. Johnson, A. N. Chan, R. D. Ward, C. A. McGlade, B. M. Hatfield, J. M. Peters and B. Li, Inhibition of Isoleucyl-tRNA Synthetase by the Hybrid Antibiotic Thiomarinol, *J. Am. Chem. Soc.*, 2021, **143**, 12003–12013.
10 D. W. Kneller, H. Li, G. Phillips, K. L. Weiss, Q. Zhang, M. A. Arnould, C. B. Jonsson, S. Surendranathan, J. Parvathareddy, M. P. Blakeley, L. Coates, J. M. Louis, P. V. Bonnesen and A. Kovalevsky, Covalent narlaprevir-

and boceprevir-derived hybrid inhibitors of SARS-CoV-2 main protease, *Nat. Commun.*, 2022, **13**, 2268.
11 W. Poon, B. R. Kingston, B. Ouyang, W. Ngo and W. C. W. Chan, A framework for designing delivery systems, *Nat. Nanotechnol.*, 2020, **15**, 819–829.
12 M. T. Manzari, Y. Shamay, H. Kiguchi, N. Rosen, M. Scaltriti and D. A. Heller, Targeted drug delivery strategies for precision medicines, *Nat. Rev. Mater.*, 2021, **6**, 351–370.
13 M. J. Mitchell, M. M. Billingsley, R. M. Haley, M. E. Wechsler, N. A. Peppas and R. Langer, Engineering precision nanoparticles for drug delivery, *Nat. Rev. Drug Discovery*, 2021, **20**, 101–124.
14 A. M. Vargason, A. C. Anselmo and S. Mitragotri, The evolution of commercial drug delivery technologies, *Nat. Biomed. Eng.*, 2021, **5**, 951–967.
15 Y. Zhao, F. Fay, S. Hak, J. Manuel Perez-Aguilar, B. L. Sanchez-Gaytan, B. Goode, R. Duivenvoorden, C. de Lange Davies, A. Bjørkøy, H. Weinstein, Z. A. Fayad, C. Pérez-Medina and W. J. M. Mulder, Augmenting drug–carrier compatibility improves tumour nanotherapy efficacy, *Nat. Commun.*, 2016, **7**, 11221.
16 J.-C. Leroux, Editorial: Drug Delivery: Too Much Complexity, Not Enough Reproducibility?, *Angew. Chem., Int. Ed.*, 2017, **56**, 15170–15171.
17 S. Shen, Y. Wu, Y. Liu and D. Wu, High drug-loading nanomedicines: progress, current status, and prospects, *Int. J. Nanomed.*, 2017, **12**, 4085–4109.
18 L. Zhu, Y. Guo, Q. Qian, D. Yan, Y. Li, X. Zhu and C. Zhang, Carrier-Free Delivery of Precise Drug–Chemogene Conjugates for Synergistic Treatment of Drug-Resistant Cancer, *Angew. Chem., Int. Ed.*, 2020, **59**, 17944–17950.
19 D. Reker, Y. Rybakova, A. R. Kirtane, R. Cao, J. W. Yang, N. Navamajiti, A. Gardner, R. M. Zhang, T. Esfandiary, J. L'Heureux, T. von Erlach, E. M. Smekalova, D. Leboeuf, K. Hess, A. Lopes, J. Rogner, J. Collins, S. M. Tamang, K. Ishida, P. Chamberlain, D. Yun, A. Lytton-Jean, C. K. Soule, J. H. Cheah, A. M. Hayward, R. Langer and G. Traverso, Computationally guided high-throughput design of self-assembling drug nanoparticles, *Nat. Nanotechnol.*, 2021, **16**, 725–733.
20 Z. Zhou, C. Du, Q. Zhang, G. Yu, F. Zhang and X. Chen, Exquisite Vesicular Nanomedicine by Paclitaxel Mediated Co-assembly with Camptothecin Prodrug, *Angew. Chem., Int. Ed.*, 2021, **60**, 21033–21039.
21 T. Liu, L. Li, S. Wang, F. Dong, S. Zuo, J. Song, X. Wang, Q. Lu, H. Wang, H. Zhang, M. Cheng, X. Liu, Z. He, B. Sun and J. Sun, Hybrid chalcogen bonds in prodrug nanoassemblies provides dual redox-responsivity in the tumor microenvironment, *Nat. Commun.*, 2022, **13**, 7228.
22 K. Yang, S. Qi, X. Yu, B. Bai, X. Zhang, Z. Mao, F. Huang and G. Yu, A Hybrid Supramolecular Polymeric Nanomedicine for Cascade-Amplified Synergetic Cancer Therapy, *Angew. Chem., Int. Ed.*, 2022, **61**, e202203786.
23 F. Fang, S. Wang, Y. Song, M. Sun, W.-C. Chen, D. Zhao and J. Zhang, Continuous Spatiotemporal Therapy of A Full-API Nanodrug via Multi-Step Tandem Endogenous Biosynthesis, *Nat. Commun.*, 2023, **14**, 1660.
24 J. Xu, J. Tan, C. Song, G. Zhang, X. Hu and S. Liu, Self-Immolative Amphiphilic Poly(ferrocenes) for Synergistic Amplification of Oxidative Stress in Tumor Therapy, *Angew. Chem., Int. Ed.*, 2023, **62**, e202303829.
25 H. Zhang, Z. Zhao, S. Sun, S. Zhang, Y. Wang, X. Zhang, J. Sun, Z. He, S. Zhang and C. Luo, Molecularly self-fueled nano-penetrator for nonpharmaceutical treatment of thrombosis and ischemic stroke, *Nat. Commun.*, 2023, **14**, 255.
26 S.-Y. Qin, A.-Q. Zhang, S.-X. Cheng, L. Rong and X.-Z. Zhang, Drug self-delivery systems for cancer therapy, *Biomaterials*, 2017, **112**, 234–247.
27 X.-Q. Zhou, P. Wang, V. Ramu, L. Zhang, S. Jiang, X. Li, S. Abyar, P. Papadopoulou, Y. Shao, L. Bretin, M. A. Siegler, F. Buda, A. Kros, J. Fan, X. Peng, W. Sun and S. Bonnet, In vivo metallophilic self-assembly of a light-activated anticancer drug, *Nat. Chem.*, 2023, **15**, 980–987.
28 H. Wang, D. Yu, J. Fang, Y. Zhou, D. Li, Z. Liu, J. Ren and X. Qu, Phenol-like group functionalized graphene quantum dots structurally mimicking natural antioxidants for highly efficient acute kidney injury treatment, *Chem. Sci.*, 2020, **11**, 12721–12730.
29 B.-C. Lee, J. Y. Lee, J. Kim, J. M. Yoo, I. Kang, J.-J. Kim, N. Shin, D. J. Kim, S. W. Choi, D. Kim, B. H. Hong and K.-S. Kang, Graphene quantum dots as anti-inflammatory therapy for colitis, *Sci. Adv.*, 2020, **6**, eaaz2630.
30 L. Đorđević, F. Arcudi, M. Cacioppo and M. Prato, A multifunctional chemical toolbox to engineer carbon dots for biomedical and energy applications, *Nat. Nanotechnol.*, 2022, **17**, 112–130.
31 W. Gao, J. He, L. Chen, X. Meng, Y. Ma, L. Cheng, K. Tu, X. Gao, C. Liu, M. Zhang, K. Fan, D.-W. Pang and X. Yan, Deciphering the catalytic mechanism of superoxide dismutase activity of carbon dot nanozyme, *Nat. Commun.*, 2023, **14**, 160.
32 W. Su, M. Tan, Z. Wang, J. Zhang, W. Huang, H. Song, X. Wang, H. Ran, Y. Gao, G. Nie and H. Wang, Targeted Degradation of PD-L1 and Activation of the STING Pathway by Carbon-Dot-Based PROTACs for Cancer Immunotherapy, *Angew. Chem., Int. Ed.*, 2023, **62**, e202218128.
33 C. Xia, S. Zhu, T. Feng, M. Yang and B. Yang, Evolution and Synthesis of Carbon Dots: From Carbon Dots to Carbonized Polymer Dots, *Adv. Sci.*, 2019, **6**, 1901316.
34 S. Li, W. Su, H. Wu, T. Yuan, C. Yuan, J. Liu, G. Deng, X. Gao, Z. Chen, Y. Bao, F. Yuan, S. Zhou, H. Tan, Y. Li, X. Li, L. Fan, J. Zhu, A. T. Chen, F. Liu, Y. Zhou, M. Li, X. Zhai and J. Zhou, Targeted tumour theranostics in mice via carbon quantum dots structurally mimicking large amino acids, *Nat. Biomed. Eng.*, 2020, **4**, 704–716.
35 Y. Xu, B. Wang, M. Zhang, J. Zhang, Y. Li, P. Jia, H. Zhang, L. Duan, Y. Li, Y. Li, X. Qu, S. Wang, D. Liu, W. Zhou, H. Zhao, H. Zhang, L. Chen, X. An, S. Lu and S. Zhang, Carbon Dots as a Potential Therapeutic Agent for the Treatment of Cancer-Related Anemia, *Adv. Mater.*, 2022, **34**, 2200905.

36 R. Qin, S. Li, Y. Qiu, Y. Feng, Y. Liu, D. Ding, L. Xu, X. Ma, W. Sun and H. Chen, Carbonized paramagnetic complexes of Mn (II) as contrast agents for precise magnetic resonance imaging of sub-millimeter-sized orthotopic tumors, *Nat. Commun.*, 2022, **13**, 1938.

37 H. Wang, X. Liu, X. Yan, J. Fan, D. Li, J. Ren and X. Qu, A MXene-derived redox homeostasis regulator perturbs the Nrf2 antioxidant program for reinforced sonodynamic therapy, *Chem. Sci.*, 2022, **13**, 6704–6714.

38 B. Geng, J. Hu, Y. Li, S. Feng, D. Pan, L. Feng and L. Shen, Near-infrared phosphorescent carbon dots for sonodynamic precision tumor therapy, *Nat. Commun.*, 2022, **13**, 5735.

39 S. Di Noja, F. Amato, F. Zinna, L. Di Bari, G. Ragazzon and M. Prato, Transfer of Axial Chirality to the Nanoscale Endows Carbon Nanodots with Circularly Polarized Luminescence, *Angew. Chem., Int. Ed.*, 2022, **61**, e202202397.

40 Z. Wang, P. Zhang, C. Yin, Y. Li, Z. Liao, C. Yang, H. Liu, W. Wang, C. Fan, D. Sun and L. Cheng, Antibiotic-Derived Carbon-Nanodot-Decorated Hydrogel for Reactive Oxygen Species-Enhanced Anti-Infection Through Biofilm Damage, *Adv. Funct. Mater.*, 2023, **33**, 2300341.

41 J. Li, J. Ma, H. Sun, M. Yu, H. Wang, Q. Meng, Z. Li, D. Liu, J. Bai, G. Liu, X. Xing, F. Han and B. Li, Transformation of arginine into zero-dimensional nanomaterial endows the material with antibacterial and osteoinductive activity, *Sci. Adv.*, 2023, **9**, eadf8645.

42 H. E. Førde, L. Sleire, H. Espedal, J. I. Heggdal, F. Selheim, P.-H. Pedersen and P. Ø. Enger, Abstract 3048: Drug repurposing: Validation of sulfasalazine as a radiosensitizer in melanoma by blocking system Xc^-, *Cancer Res.*, 2016, **76**, 3048.

43 W. Wang, M. Green, J. E. Choi, M. Gijón, P. D. Kennedy, J. K. Johnson, P. Liao, X. Lang, I. Kryczek, A. Sell, H. Xia, J. Zhou, G. Li, J. Li, W. Li, S. Wei, L. Vatan, H. Zhang, W. Szeliga, W. Gu, R. Liu, T. S. Lawrence, C. Lamb, Y. Tanno, M. Cieslik, E. Stone, G. Georgiou, T. A. Chan, A. Chinnaiyan and W. Zou, CD8+ T cells regulate tumour ferroptosis during cancer immunotherapy, *Nature*, 2019, **569**, 270–274.

44 M. A. Badgley, D. M. Kremer, H. C. Maurer, K. E. DelGiorno, H.-J. Lee, V. Purohit, I. R. Sagalovskiy, A. Ma, J. Kapilian, C. E. M. Firl, A. R. Decker, S. A. Sastra, C. F. Palermo, L. R. Andrade, P. Sajjakulnukit, L. Zhang, Z. P. Tolstyka, T. Hirschhorn, C. Lamb, T. Liu, W. Gu, E. S. Seeley, E. Stone, G. Georgiou, U. Manor, A. Iuga, G. M. Wahl, B. R. Stockwell, C. A. Lyssiotis and K. P. Olive, Cysteine depletion induces pancreatic tumor ferroptosis in mice, *Science*, 2020, **368**, 85–89.

45 S. Bekeschus, S. Eisenmann, S. K. Sagwal, Y. Bodnar, J. Moritz, B. Poschkamp, I. Stoffels, S. Emmert, M. Madesh, K.-D. Weltmann, T. von Woedtke and R. K. Gandhirajan, xCT (SLC7A11) expression confers intrinsic resistance to physical plasma treatment in tumor cells, *Redox Biol.*, 2020, **30**, 101423.

46 Z. Shen, J. Song, B. C. Yung, Z. Zhou, A. Wu and X. Chen, Emerging Strategies of Cancer Therapy Based on Ferroptosis, *Adv. Mater.*, 2018, **30**, 1704007.

47 S. Liang, X. Deng, P. a. Ma, Z. Cheng and J. Lin, Recent Advances in Nanomaterial-Assisted Combinational Sonodynamic Cancer Therapy, *Adv. Mater.*, 2020, **32**, 2003214.

48 G. Xu, C. Li, C. Chi, L. Wu, Y. Sun, J. Zhao, X.-H. Xia and S. Gou, A supramolecular photosensitizer derived from an Arene-Ru(II) complex self-assembly for NIR activated photodynamic and photothermal therapy, *Nat. Commun.*, 2022, **13**, 3064.

49 D. T. Sawyer and J. S. Valentine, How super is superoxide?, *Acc. Chem. Res.*, 1981, **14**, 393–400.

50 W. H. Koppenol, D. M. Stanbury and P. L. Bounds, Electrode potentials of partially reduced oxygen species, from dioxygen to water, *Free Radical Biol. Med.*, 2010, **49**, 317–322.

51 L. Wang, R. Leite de Oliveira, S. Huijberts, E. Bosdriesz, N. Pencheva, D. Brunen, A. Bosma, J.-Y. Song, J. Zevenhoven, G. T. Los-de Vries, H. Horlings, B. Nuijen, J. H. Beijnen, J. H. M. Schellens and R. Bernards, An Acquired Vulnerability of Drug-Resistant Melanoma with Therapeutic Potential, *Cell*, 2018, **173**, 1413–1425.

52 Y. Zhang, R. V. Swanda, L. Nie, X. Liu, C. Wang, H. Lee, G. Lei, C. Mao, P. Koppula, W. Cheng, J. Zhang, Z. Xiao, L. Zhuang, B. Fang, J. Chen, S.-B. Qian and B. Gan, mTORC1 couples cyst(e)ine availability with GPX4 protein synthesis and ferroptosis regulation, *Nat. Commun.*, 2021, **12**, 1589.

53 Z. Shi, N. Naowarojna, Z. Pan and Y. Zou, Multifaceted mechanisms mediating cystine starvation-induced ferroptosis, *Nat. Commun.*, 2021, **12**, 4792.

54 X. Song, S. Zhu, P. Chen, W. Hou, Q. Wen, J. Liu, Y. Xie, J. Liu, D. J. Klionsky, G. Kroemer, M. T. Lotze, H. J. Zeh, R. Kang and D. Tang, AMPK-Mediated BECN1 Phosphorylation Promotes Ferroptosis by Directly Blocking System Xc– Activity, *Curr. Biol.*, 2018, **28**, 2388–2399.